On the Equilibrium Spectrum of Transient Waves in the Atmosphere

WENDELL T. WELCH

Advanced Study Program, National Center for Atmospheric Research, Boulder, Colorado*

KA-KIT TUNG

Department of Applied Mathematics, University of Washington, Seattle, Washington

(Manuscript received 14 April 1997, in final form 6 November 1997)

ABSTRACT

The spectrum of transient heat flux in the midlatitude troposphere has a maximum at a synoptic scale. The same is true of the transient energy. The wavenumber of these maxima can be explained by the theory of nonlinear baroclinic adjustment, which is also shown to predict the shape of the spectra.

According to this theory, each zonal wave has a nonlinear threshold that bounds its growth, and the bounds are larger for longer waves. The most unstable wave grows and transports heat until it reaches its threshold, at which point it breaks and saturates, passing off excess energy to the next longer wave. The process repeats, with energy cascading upscale, until the total heat transport is sufficient to reduce the meridional temperature gradient down to a relatively constant equilibrium level, independent of forcing. Thus at higher forcings more heat must be transported and the cascade extends to longer scales. At equilibrium, the longest heat-transporting wave has not saturated but rather has been rendered linearly neutral by the reduction in the temperature gradient.

Observations from the real atmosphere, and computations with a quasigeostrophic two-level model in a beta-plane channel, corroborate the theory presented.

1. Introduction

The behavior of transient eddies in the midlatitudes yields a maximum of heat flux at a synoptic scale. This is shown for the different seasons and hemispheres in Fig. 1 (redrawn from Fig. 2 of Randel and Held 1991). A similar peak at synoptic scales is found in the spectrum of transient energy (discussed later). Various theories have been proposed to explain the presence of this synoptic maximum of heat flux or energy.

The synoptic peak has been identified with baroclinic instability, for observations of the dominant eddies in the atmosphere have shown them to be of synoptic scale and baroclinic in nature (Charney 1971). The simplest explanation for their dominance would be linear: the most unstable wave from a linear analysis of the zonally averaged atmosphere would dominate the spectrum. For example, Stone (1978) proposed a theory of ''baroclinic adjustment'' in which he argued that the most unstable wave in a two-level model would do all of the heat transport at equilibrium. However, simulations in Welch and Tung (1998) showed that, when nonlinear interactions between waves are included in such a model, a longer wave emerges as dominant. This is found in the real atmosphere as well. Gall (1976) determined that the linearly most unstable waves in a continuous atmosphere are zonal wavenumbers 12–15, with maxima near the surface of the earth. Meanwhile, the transient eddies that dominate in the real (nonlinear) atmosphere are wavenumbers 4–7 (as in Fig. 1) and have largest amplitude near the tropopause (Gall 1976). Thus a linear explanation predicts the wrong wave as dominant and hence is unable to account for the synoptic energy maximum.

To reconcile for this discrepancy, a nonlinear upscale cascade of energy, as presented in the geostrophic turbulence study of Charney (1971), is often cited. Salmon (1980) united Charney's upscale cascade with the concept of energy injection at synoptic scales due to baroclinic instability. He argued for a balance at the short scales between energy extraction from the mean flow and nonlinear transfer toward long scales. Such dynamics could yield an energy maximum at a synoptic scale that is longer than that of the most unstable wave.

Salmon's theory, however, does not explain why or how a particular wavenumber comes to dominate either the energy or the heat flux spectrum. For example, it cannot explain why in Fig. 1, in the Southern Hemi-

* The National Center for Atmospheric Research is sponsored by the National Science Foundation.

Corresponding author address: Dr. Wendell T. Welch, NCAR/ASP, P.O. Box 3000, Boulder, CO 80307-3000.
E-mail: welch@ucar.edu

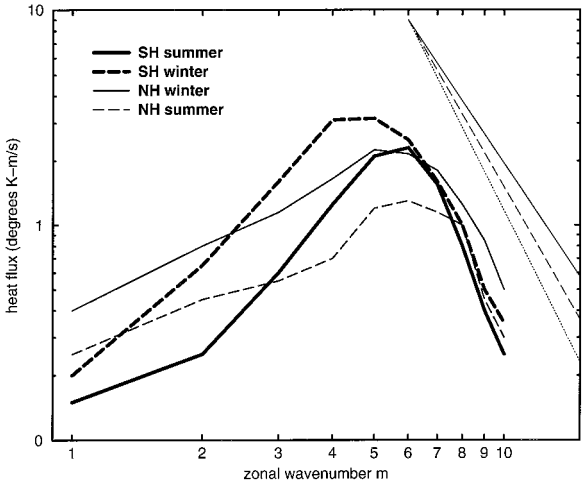

FIG. 1. Observed spectra of transient eddy heat flux vs nondimensional zonal wavenumber m for the different seasons and hemispheres. Each point represents the heat flux ($\overline{v'_m T'_m}$) at 47° and 700 mb. Redrawn from Randel and Held (1991). For comparison, lines of slope -3 (thin solid), -3.5 (thin dashed), and -4 (thin dotted) have been included in this log–log plot.

sphere summer (thick solid line), there is a maximum of heat flux at the synoptic zonal wavenumber $m = 6$. Why does the cascade not continue to a longer (or shorter) scale? Why in the Southern Hemisphere winter (thick dashed line) is the maximum at the longer wave $m = 5$? Also, given this seasonal shift in the peak wavenumber, why is the heat flux for the shorter waves $m \geq 6$ the *same* season to season? Can the wavenumber of maximum heat flux, and the shape of the spectrum, be predicted? Can such predictions be made for any climate? Can the same be done for the energy spectrum?

Rhines (1975) proposed a theory for the selection of the peak wavenumber. He reasoned that Charney's cascade would dominate at small scales, whereas linear Rossby wave dynamics would be present for the largest waves. At the scale where these two mechanisms have roughly the same magnitude, Rhines said the cascade would stop, and there the energy would be a maximum. He offered a formula for calculating this dominant ''wavenumber of cascade arrest.'' However, his theory is not predictive, requiring information about the root-mean-square wave speed at equilibrium. A formula to predict which wave will dominate at equilibrium, based only on external parameters, still needs to be derived.

Here we will show that the theory of nonlinear baroclinic adjustment (Cehelsky and Tung 1991; Welch and Tung 1998) can answer the above questions. The theory has two main points. First, for a given solar forcing (i.e., imposed meridional temperature gradient), there is a certain amount of heat that must be transported poleward in order to equilibrate the system, and the magnitude of this heat transport rises linearly with the forcing. Second, each wave has a nonlinear threshold, above which it can no longer grow or transport heat, and the thresholds increase with the zonal wavelength. With these two precepts, we can explain which wavenumber dominates at equilibrium for any level of forcing and why for most forcings this wave must be longer than that most unstable. Furthermore, we can predict the shape of the spectra of heat flux and of energy for synoptic transient waves in the midlatitude troposphere.

We will verify our theory by comparing its predictions with observations of heat flux, and also by using simulations from a high-resolution two-level quasi-geostrophic baroclinic model in a β-plane channel with a flat bottom. Although simple, the model can be validated by comparing its heat flux spectrum and meridional temperature gradient with those from the real midlatitude troposphere. It will be shown that the model simulations match the magnitude and shape of observed spectra, as well as the magnitude of observed temperature gradients, for both winter and summer seasons. Moreover, the model accurately simulates the shift in peak wavenumber from 6 to 5, winter to summer, that is shown in Fig. 1.

In section 2 the nonlinear baroclinic adjustment theory will be reviewed and then used to explain the spectrum of transient heat flux, including its peak wavenumber and shape. Such explanations will then be applied to the transient energy spectrum. In section 3 these predictions will be compared with model simulations and observations. Alternate theories by Rhines, Salmon, James, Farrell, and Lindzen are discussed in section 4, and numerical modeling issues in section 5. Section 6 contains conclusions.

2. Nonlinear baroclinic adjustment

a. Selection of the dominant heat-transporting wave

To explain the synoptic peak in the transient heat flux spectrum, we will use the theory of nonlinear baroclinic adjustment. This theory was introduced in the study of Cehelsky and Tung (1991) and elaborated by Welch and Tung (1998). Here we will review the concept and show how it determines the wave scale of maximum heat transport.

Nonlinear baroclinic adjustment is motivated by the recognition of an ''atmospheric thermostat.'' There seems to be a mechanism that maintains the midlatitude temperature gradient in the middle troposphere at a fairly constant value season to season (Stone 1978). This is true even though the radiative forcing varies considerably with the seasons. This implies that there must be a flexible component of the system that moderates the imposed forcing, responding more for higher forcings and less for lower. The theory posits that this flexible component is the meridional heat transport of baroclinically unstable waves excited by the temperature gradient. For a given level of forcing, there must be a certain amount of heat that the sum of *all* baroclinically unstable waves transport poleward. The total amount of

heat transported must increase linearly with the forcing so that the temperature gradient that results is about the same regardless of forcing.

Note that the theory does not assume that the heat is transported by the most unstable wave alone, which was Stone's (1978) original proposal of *linear* baroclinic adjustment. He argued that no other waves would participate because they would be linearly stabilized by the action of the most unstable wave, which would reduce the flow to the minimum critical shear or temperature gradient. In the theory of *nonlinear* baroclinic adjustment, the heat transport is spread over many scales, and the wave that ends up dominating this process at equilibrium is usually not the most unstable wave.

The rule determining how heat transport is distributed among the various wavelengths is based on the concept of a nonlinear threshold for each wave, above which it can no longer grow. At this limiting magnitude, the wave will break and saturate, shedding excess energy to other scales.

This idea is motivated by the criterion for instability given by the Charney–Stern theorem: if the background potential vorticity gradient $\overline{Q}_y$ is negative somewhere in the fluid, then the fluid may be unstable to small-scale secondary perturbations (Charney and Stern 1962). (Here Q is the potential vorticity (PV), y is the north–south coordinate, and the overbar represents a zonal mean.) This theorem was derived for the case of a zonally uniform flow, and here we simply extend it to include the contribution from a synoptic or planetary scale heat-transporting wave. That is, we claim that when the *total* PV gradient $Q_y = \overline{Q}_y + Q'_y$ becomes negative, the flow becomes unstable. (A prime indicates deviation from the zonal mean state.) The dominant wave then breaks and cannot grow further.

We can show that this generalized Charney–Stern theorem translates into a nonlinear threshold of heat transport for each wave. By definition, the wavy component of PV gradient oscillates in sign with longitude. If its magnitude is large enough, then in its negative phase it will outweigh the zonal-mean gradient and render the total PV gradient negative. Hence the above condition for instability can be rewritten as $|Q'_y| > \overline{Q}_y$ (Garcia 1991). At such a magnitude, the wave will break and no longer gain amplitude. This yields the following criterion for saturation:

$$|Q'_y| \approx \overline{Q}_y. \tag{2.1}$$

The magnitude of $\overline{Q}_y$ does not change sign with forcing. To see this, consider the (dimensional) quasigeostrophic PV:

$$Q \equiv f_0 + \beta_0 y + \nabla^2\Psi + \frac{f_0^2}{N^2}\frac{\partial^2\Psi}{\partial z^2}. \tag{2.2}$$

Here Ψ is the streamfunction, from which velocities are given by $\mathbf{u} = \mathbf{k} \times \nabla\Psi$; $f_0 + \beta_0 y$ is the Coriolis force in a beta-plane approximation, N is the Brunt–Väisälä frequency, and z is the vertical coordinate. Using the hydrostatic equation, the equilibrated zonal average can be approximated:

$$\overline{Q} \approx f_0 + \beta_0 y + \frac{f_0 R}{N^2 H}\frac{\partial \overline{T}}{\partial z}, \tag{2.3}$$

where R is the ideal gas constant, H the density-scale height of the atmosphere, and $\overline{T}$ is the zonal mean temperature. Here the relative vorticity $-\overline{U}_y$ has been neglected because it is usually small compared to the planetary component (as confirmed by model simulations). The meridional gradient of zonal mean PV is, then,

$$\overline{Q}_y \approx \beta_0 + \frac{f_0 R}{N^2 H}\frac{\partial}{\partial z}\left(\frac{\partial \overline{T}}{\partial y}\right). \tag{2.4}$$

It has already been mentioned that the meridional temperature gradient is fairly robust in the midtroposphere, even as the forcing changes dramatically from season to season (Stone 1978). We expect the vertical derivative to be similarly robust, and hence $\overline{Q}_y$ as well.

Because $\overline{Q}_y$ is independent of forcing, it can provide a limit on the magnitude of Q'_y by (2.1). This relation gives an order of magnitude estimate for the size of Q'_y for any saturated wave, regardless of the level of forcing. Model results do show a weak dependence of $|Q'_y|$ on zonal wavenumber m, but still a good rule of thumb is that each wave can generate a PV gradient only about as large as the zonal mean gradient.[1]

The limit on $|Q'_y|$ can be translated into a limit on heat flux for each wave. This was discussed in Welch and Tung (1998) for a two-level model, and here it is generalized to a continuous atmosphere. Consider a single wave with wavenumbers m, n, and μ in the zonal, meridional, and vertical directions, respectively. Assume the streamfunction has the form:

$$\Psi' = \mathrm{Re}\{Ae^{im(x-ct)}\sin ny\, e^{i\mu z}\}, \tag{2.5}$$

where all variables are dimensional and μ and c can be complex. (We assume A is real without loss of generality.) Using this form to calculate the eddy heat flux convergence Π yields

$$\begin{aligned}\Pi &\equiv -\frac{\partial}{\partial y}(\overline{v'T'}) \\ &= -\frac{f_0 H}{2R}A^2 mn\mu_r e^{2mc_i t}\sin 2ny e^{-2\mu_i z}.\end{aligned} \tag{2.6}$$

Thus, we see that

$$|\Pi| = \frac{f_0 H}{2R}mn|\Psi'|^2|\mu_r|. \tag{2.7}$$

Here μ_r is the real part of μ, which from (2.5) can be

[1] Strickly speaking, it is the sum of all waves' PV gradients that is capped by $\overline{Q}_y$. However, the differing phases and wavelengths sufficiently inhibit such overlap that each wave can be considered to be limited independently.

seen to measure how rapidly the phase of the wave changes with height, that is, the vertical phase tilt. This phase tilt is only a weak function of wavenumber, as will be shown in section 2b.

Also using (2.5) we can develop an expression for the meridional gradient of potential vorticity in wave (m, n). Differentiating the wavy part of (2.2) gives

$$(Q_y') = \frac{\partial}{\partial y}\left[\nabla^2\Psi' + \frac{f_0^2}{N^2}\frac{\partial^2}{\partial z^2}\Psi'\right] = \mathrm{Re}\left\{n\left(-m^2 - n^2 - \frac{f_0^2}{N^2}\mu^2\right)Ae^{-im(x-ct)}\cos nye^{i\mu z}\right\}. \tag{2.8}$$

Thus, we have

$$|(Q_y')| = n\left(m^2 + n^2 + \frac{f_0^2}{N^2}\mu^2\right)|\Psi'| \approx n(m^2 + n^2)|\Psi'|. \tag{2.9}$$

Combining (2.7) and (2.9) together yields

$$|(Q_y')| \approx \sqrt{\frac{2R}{f_0 H}\frac{n(m^2 + n^2)^2}{m|\mu_r|}}\sqrt{|\Pi|} \approx \sqrt{\frac{2R}{f_0 H}\frac{nm^3}{|\mu_r|}}\sqrt{|\Pi|} \tag{2.10}$$

for synoptic-scale modes ($m \geq 4$), given that long meridional wavelengths are typically dominant. When summed over all meridional contributions n, this relation can be approximated asymptotically as[2]

$$|(Q_y')| \sim K\sqrt{\frac{m^3}{|\mu_r|}}\sqrt{|\Pi|}, \tag{2.11}$$

where K represents the constant factor $\sqrt{2R/f_0 H}$ in (2.10). Using (2.1) to limit the size of the wavy PV gradient and using (2.4) yields

$$|\Pi|(m) \sim Km^{-3}|\mu_r|\,|(Q_y')|^2 \sim Km^{-3}|\mu_r|(\overline{Q}_y)^2 \sim Km^{-3}|\mu_r|\left[\beta_0 + \frac{f_0 R}{N^2 H}\frac{\partial}{\partial z}\left(\frac{\partial\overline{T}}{\partial y}\right)\right]^2, \tag{2.12}$$

where K has been redefined. (This expression has been derived for m dimensional, but it holds as well for nondimensional m if K is adjusted.) Thus, we have given reason for a saturation limit or threshold for the amount of heat that can be transported by each wave, a limit that depends on zonal wavenumber but is independent of forcing. Including the m^{-1} asymptotic dependence of phase tilt to be derived below, this formula shows that heat transport for saturated waves varies with wavenumber as m^{-4}. The overall effect of (2.12) is that saturation thresholds are lower for shorter waves.

Note that this formula represents a spectrum of *saturated* waves. A particular spectrum from the real atmosphere, or a model simulation, is expected to approach this shape asymptotically as waves near saturation; that is, as m gets larger.

With these thresholds in mind, we can now return to the question of how the heat transport is distributed among the different zonal waves. For a given forcing, a certain amount of heat must be transported to reach the robust equilibrium. If this exceeds the threshold of the most unstable wave (as it often does by a wide margin), then that wave will break and the excess heat will be taken up by the next longer wave because it has a higher threshold. If this next longer wave reaches *its* threshold, then it will break and shed its excess energy. This process will continue until the total heat that must be transported has been accounted for, and thus the heat will be spread over a spectrum of baroclinic waves. Notice that the relationship (2.12) gives another argument for the *upscale* cascade of Charney (1971). Energy cannot cascade to a shorter scale, even if that scale is linearly unstable, for it has a nonlinear threshold that is even smaller than that of the saturating wave.

When an unstable wave reaches its saturation level, it is ''nonlinearly stabilized'' by sending energy to other scales. The longest wave to transport heat, however, will not have reached its threshold, and hence it will not be stabilized nonlinearly at equilibrium. Rather, it stabilizes itself. Through its heat transport, it reduces the zonal mean temperature gradient to a level at which it is linearly neutral, in the manner Stone envisioned for the most unstable wave.

It is this last wave that acts as the atmospheric thermostat. It is the flexible component of the system, determining the equilibrium temperature gradient essentially by itself via a quasi-linear mechanism. In most cases this wave does the bulk of the heat transport and thus we call it the dominant heat-transporting wave. For all but the smallest forcings, this wave will be longer than the most unstable wave, the latter having been nonlinearly saturated.

The reason that the cascade does not continue further upscale is that all the necessary heat transport has been borne by the shorter waves. There appears to be an ''objective'': to transport just enough heat to maintain the atmospheric ''thermostat.'' When that objective is achieved, no further upscale cascade is needed, and thus it stops at the scale of the dominant heat-transporting wave. The dominant wave then reduces the temperature gradient such that longer waves are linearly stabilized and do not participate in the dynamics. This equilibration process depends on the radiative driving. For higher forcing, more heat flux will be required and hence more

[2] This is the dimensional, continuous atmosphere equivalent of Eq. (4.5) in Welch and Tung (1998).

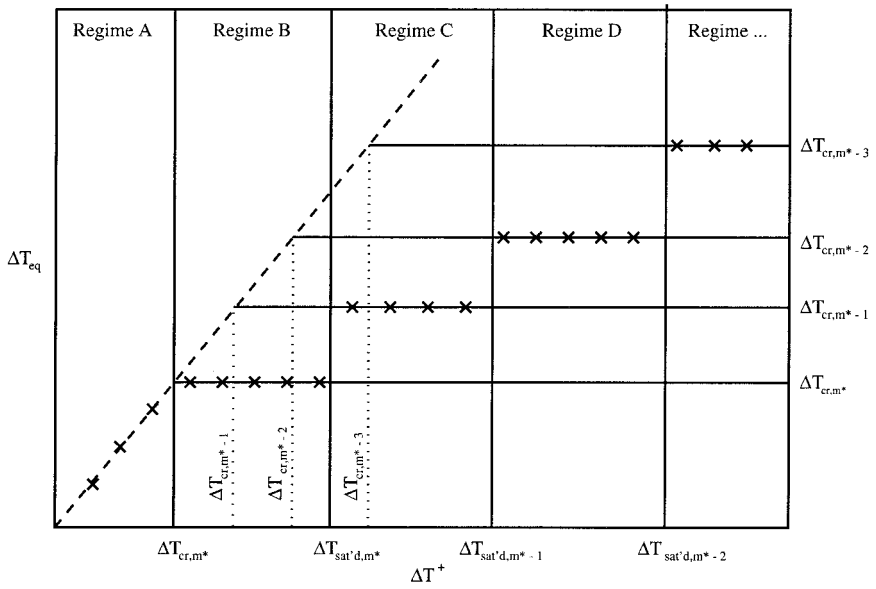

FIG. 2. Conceptual model of nonlinear baroclinic adjustment for a geometry with many linearly unstable waves. The most unstable is given (nondimensionally) by m^*. Equilibrium temperature gradients are indicated by crosses; the Hadley solution is given by a dashed line. Solid horizontal lines (and dotted vertical lines) indicate $\Delta\overline{T}_{cr}$ for different zonal wavenumbers. Solid vertical lines are regime boundaries.

waves needed to transport heat to achieve equilibrium. The cascade will continue until a longer wave is selected as dominant.

Our theory is summarized in the schematic diagram of Fig. 2. The crosses indicate the equilibrated temperature gradient over a range of forcing levels, and the most unstable wave is denoted as m^*. For low forcings, the temperature gradient equilibrates at that of the Hadley solution (dashed line), for no waves are unstable and thus there is no heat transport. For slightly higher forcings, m^* becomes unstable and grows, transporting heat and reducing the temperature gradient down to a level at which that wave is just critical. As the forcing is raised, m^* will reach its nonlinear threshold, at which point it will saturate and break, and the next longer, next most unstable wave ($m^* - 1$) will take over the flexible role. This wave will then reduce the temperature gradient down to *its* critical level, until at a high enough forcing it also breaks. This process repeats for longer and longer waves as the forcing is raised.

Notice that what determines when the temperature gradient shifts to a new regime is not when waves reach their critical gradients from a linear stability analysis, but rather when they reach their nonlinear saturation levels. Also, the schematic has an exaggerated ordinate for clarity; the critical gradients of the various waves should be much closer in magnitude. This would yield a relatively constant temperature gradient over a range of forcings, as found in observations (Stone 1978).

We have explained the selection of the dominant heat-transporting mode. Now let us address the shape of the heat transport spectrum by completing the relation (2.12) with a discussion of the vertical phase tilt.

b. Shape of the transient heat flux spectrum

The magnitude of the heat flux, given by (2.7), involves the magnitude of the phase tilt of the wave, which we have already claimed is weak: only $O(m^{-1})$ for shorter waves. This can be determined by considering a linear wave in a vertically continuous atmosphere. The dispersion relation shows that phase tilt μ_r is proportional to growth rate c_i for shorter synoptic waves (see below). As the waves get longer this dependence lessens. Now linear waves by definition have exponential growth, which we assume is balanced by dissipation, which means that in (2.5) $mc_i \approx$ damping rate, giving $c_i \sim 1/m$. Therefore, for shorter waves we have $\mu_r \sim c_i \sim m^{-1}$, while $\mu_r \to m^0$ as $m \to 0$.

We can now write the heat flux formula (2.12) as

$$|\Pi| \sim m^{-4}. \tag{2.13}$$

This is valid asymptotically for waves as they approach saturation. Thus we expect it to be best for the shorter heat transporting waves. For the longer heat transporting waves, which are less likely to be saturated and also have a weaker dependence of phase tilt on c_i, we expect the spectrum might be slightly flatter in shape.

Let us confirm the above by showing an actual calculation. Linearizing the quasigeostrophic potential vorticity equations about a zonal-mean state profile $\overline{U}(z)$ (Charney and Drazin 1961), and using the form (2.5)

for the streamfunction, one finds the following dispersion relation:

$$\mu^2 = -\frac{N^2}{f_0^2}(m^2 + n^2) + \frac{N^2}{f_0^2}\frac{\beta_0 + \frac{f_0^2}{N^2H}\overline{U}_z}{\overline{U} - c}$$

$$= -\left[\frac{N^2}{f_0^2}(m^2 + n^2) - \frac{N^2}{f_0^2}\frac{\hat{\beta}(\overline{U} - c_r)}{(\overline{U} - c_r)^2 + c_i^2}\right]$$

$$+ i\frac{N^2}{f_0^2}\frac{\hat{\beta}c_i}{(\overline{U} - c_r)^2 + c_i^2}, \qquad (2.14)$$

where $\hat{\beta} \equiv \beta_0 + (f_0^2/N^2H)\overline{U}_z$ and we have neglected terms in $\overline{U}_{zz}$ because they are typically small compared to β_0.

For nongrowing solutions to (2.14), the term in brackets is positive for the typical troposphere at 850 mb (the altitude of maximum heat transport; see Solomon 1997). Thus $\mu_r = 0$, and by (2.7) neutral waves transport no heat meridionally and are not of interest here.

For growing waves, the value of μ_r in (2.14) depends on c_i. As we are interested in the phase tilt and heat flux of waves *at equilibrium*, we should not use for c_i the growth rate of baroclinic waves in the rapid growth phase of their life cycle. Rather, at equilibrium their growth must be balanced by dissipative forces such as Newtonian cooling and Ekman friction. Damping timescales of these processes are roughly 20–30 days and 6 days, respectively; we would expect the growth rate of a wave at equilibrium to have a timescale somewhere in between these values. For a damping time of D days, we can calculate c_i from $mc_i = 1/D$ days for each m. Then using typical tropospheric values for the other factors in (2.14), we can calculate μ_r as a function of m. This has been plotted in Fig. 3 for three different timescales: 30, 20, and 6 days. Comparing against the thin solid line, we see that μ_r indeed falls off with the slope m^{-1} for large m. The longer waves fall off less quickly, and the longest waves' phase tilts can even grow with m. However, for the heat transporting waves ($m \geq 4$), the three curves on average decay with m, slowly for the longest waves and approaching the rate m^{-1} for shorter waves.

Thus we have verified formula (2.13) above as asymptotically correct for heat transporting waves. For the longest heat transporting waves the spectrum might be slightly flatter.[3]

c. The transient energy spectrum

The arguments used above for the transient heat flux spectrum also shed light on the spectrum of total transient energy E (kinetic plus available potential), for it has very similar features. The energy is given by

$$E = \frac{1}{2}(u'^2 + v'^2) + \frac{g^2}{2N^2T_0^2}T'^2, \qquad (2.15)$$

where g is the force due to gravity and T_0 a reference temperature. Then using the form (2.5) we have $E \sim m^2\Psi'^2$ when m is large. However, $\Pi = -\partial(\overline{v'T'})/\partial y \sim m\Psi'^2$. Therefore, one would expect energy to fall off less quickly with m than the heat flux does. From (2.13), a rough prediction would be that the shape of the energy spectrum be given by

$$E \sim m^{-3}. \qquad (2.16)$$

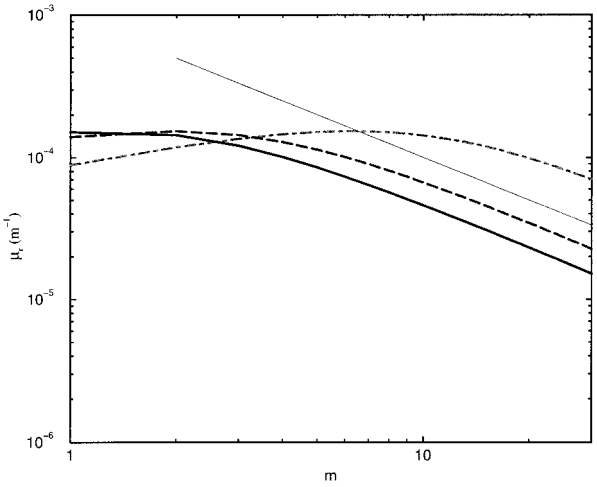

FIG. 3. Phase tilt μ_r vs (nondimensional) zonal wavenumber for a baroclinic wave in a linearized, vertically continuous atmosphere. Waves with three different equilibrium growth rates are considered: $O(30)$ days (solid curve), $O(20)$ days (dashed), and $O(6)$ days (dot–dashed). The thin solid line has slope m^{-1}.

3. Comparison of theory with numerical simulations and observations

a. Numerical model

To test the theory proposed above, we run simulations of a two-level quasigeostrophic model in a β-plane channel. The model includes Newtonian cooling to a radiative equilibrium temperature profile and Ekman friction at the earth's surface. The domain approximates the midlatitude troposphere: a channel of 45° width centered on 50°N and extending from the top of the Ekman layer to 200 mb. We assume rigid walls, and a rigid (and flat) top and bottom. The model is finite-differenced into two levels[4] in the vertical. This is the same

[3] We note that the above development is applicable not only to the continuous atmosphere but to a model with a rigid lid as well, with minor modifications to allow for standing waves.

[4] In Welch and Tung (1998) we called this same setup a two-*layer* model, because it follows from the original formulation of Lorenz (1960), which he termed the same. However, both our model and his are actually *level* models, for the height at which the variables are to be evaluated is specified. See Pedlosky (1987).

model as that developed in Welch and Tung (1997) except for the values of a few parameters, which will be discussed below.

The nondimensionalized, leveled equations in pressure coordinates are

$$\frac{\partial}{\partial t}\nabla_\delta^2\Psi_1 = -\delta J(\Psi_1, \nabla_\delta^2\Psi_1) - \delta\beta\frac{\partial\Psi_1}{\partial x} + \omega_2 - \omega_0 \tag{3.1}$$

$$\frac{\partial}{\partial t}\nabla_\delta^2\Psi_3 = -\delta J(\Psi_3, \nabla_\delta^2\Psi_3) - \delta\beta\frac{\partial\Psi_3}{\partial x} + \omega_4 - \omega_2 \tag{3.2}$$

$$\frac{\partial}{\partial t}(\Psi_3 - \Psi_1) = -\frac{1}{2}\delta J(\Psi_1 + \Psi_3, \Psi_3 - \Psi_1) - 2\sigma_0\omega_2 - 2h''[\Psi_3 - \Psi_1 - (\Psi_3 - \Psi_1)^\dagger], \tag{3.3}$$

where $\Psi = \Phi/f_0$ is the geostrophic streamfunction and $\omega = dp/dt$ is the vertical velocity. Subscripts 1 and 3 indicate the upper and lower levels, 2 the interface, and 0 and 4 the top and bottom of the model, respectively; $\nabla_\delta^2 = \delta^2(\partial^2/\partial x^2) + (\partial^2/\partial y^2)$ is the nondimensionalized Laplacian, and a † identifies the radiative forcing. Henceforth all variables (including wavenumbers m and n) are nondimensional unless otherwise noted.

Several nondimensional parameters have been introduced: β is the meridional gradient of the Coriolis parameter f, σ_0 is a measure of static stability (specified and held constant in our simulations), h'' is the relaxation timescale for the radiative forcing, and $\delta = L_y/L_x$ is a horizontal aspect ratio, where L_x and L_y indicate the scale of the domain in the zonal and meridional directions, respectively.[5] Specifying δ is equivalent to setting the length scale of the gravest zonal mode allowed (for a fixed channel width): the larger δ, the shorter the fundamental mode's wavelength. Thus, by varying δ, the number of zonal modes that are unstable can be varied.

In this study we are attempting to simulate a case akin to the real atmosphere in which many waves are unstable and participate in the baroclinic equilibration. We choose the value $\sigma_0 = 0.06$ for the static stability parameter, which is in the range 0.05–0.09 calculated from tropospheric observations (Welch 1996). We select $\delta = 0.28$ because it corresponds to a channel that circumscribes the earth, that is, to the real midlatitudes. To see this, recognize that the width of channel should correspond to the meridional range in which baroclinic disturbances occur. In the real atmosphere this is determined by the zonal jet, for it acts as a waveguide, confining baroclinic disturbances to approximately 30° of latitude. The length of the channel should correspond to one circumference of the globe at our center latitude of 50°N. Thus the dimensional width $= 2\pi R_E(30/360)$ and dimensional length $= 2\pi R_E \cos 50°$, where $R_E =$ radius of the earth, giving width/length $= 1/(12\cos 50°)$. Then $\delta = L_y/L_x =$ twice dimensional width to length $= 1/(6\cos 50°) = 0.26 \approx 0.28$.

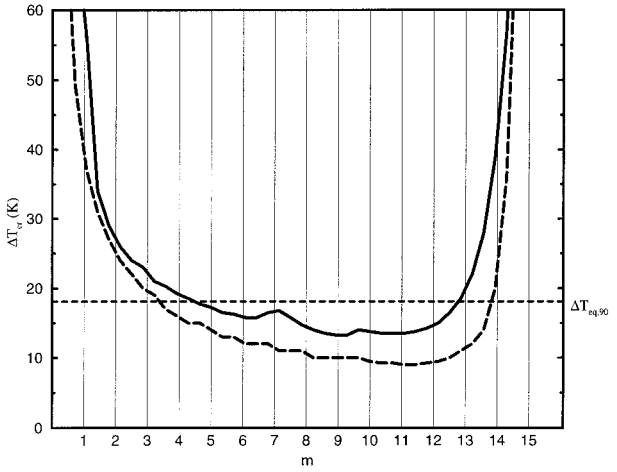

FIG. 4. Marginal stability curve, Im$\{mc_m\} = 0$, vs zonal wavenumber m for the initial state (dashed) and the equilibrium state (solid) at $\Delta T^\dagger = 90$ K. Each curve accounts for eigenfunctions of all possible meridional profiles, that is, all n. Thin vertical lines denote zonal wavenumbers $m = 1$–15 for the geometry $\delta = 0.28$. The horizontal dotted line shows the equilibrated temperature gradient $\Delta\overline{T}_{eq} \approx 18$ K for $\Delta T^\dagger = 90$ K.

Such a value of δ allows many zonal waves to be linearly unstable. This can be seen in Fig. 4, which displays the marginal stability (dashed) curve of the wave-free solution of (3.1)–(3.3). There are approximately 14 waves unstable, with the most unstable being $m = 11$. This is close to the scale of the most unstable wave in the real atmosphere [$m = 12$–15 from Gall (1976)]. Furthermore, as we shall see in the model results (Fig. 6), this geometry with a realistic forcing of $\Delta T^\dagger = 90$ K yields $m = 5$ as the dominant heat transporting wave at equilibrium, which is in the range found in observations by Randel and Held (1991). Thus with our chosen parameter values the model simulates the key baroclinic wave scales of the current atmosphere.

The solution of the model is the same as in the previous two-wave study. A ∇_δ^4-type subgrid damping term is added to the vorticity equation at each level to represent the frictional effect of small scales. The dependent variables are expanded in the eigenfunctions of the Laplacian operator in the horizontal, and an ordinary differential equation solver based on the Runge-Kutta method is used to calculate the expansion coefficients over time. Tests at various resolutions indicate that, for this case with many waves unstable, 26 modes must be retained in both the meridional and zonal directions to yield a convergent solution, and the

[5] We let the nondimensional variable $\hat{x}$ range over $[0, 2\pi]$, whereas $\hat{y}$ only ranges over $[0, \pi]$. The latter is due to our choice of sinny as the meridional eigenfunctions in order to satisfy the no-flow sidewall boundary conditions. Thus δ is twice the ratio of the dimensional width to length. See Welch (1996).

simulations must be carried out for approximately one year (3000 nondimensional time steps) and averaged over the last four months (1000 time steps). All experiments in the subsequent discussions were run in this way, starting from the Hadley state (the wave-free solution of the above equations of motion), with all zonal and meridional wavenumbers perturbed with random but small magnitude.

For further details of the model see Welch (1996). It is formulated the same as that in the original study of Cehelsky and Tung (1991), except for a few parameter values and for a now more efficient method to calculate the nonlinear terms. Most importantly; to simulate the real atmosphere requires many waves to be unstable, and hence a higher resolution was needed than the original model study could provide (10×10). The current model is the same as that used in Welch and Tung (1998); we have simply used a smaller value of the aspect ratio δ here to yield more waves unstable.

b. Model output

We will measure the modeled climate in several ways. One simple measure is the zonally averaged temperature difference (or ''gradient'') across the midlatitudes in the middle troposphere, which we label $\Delta\overline{T}_2$. An expression for this can be derived by zonally averaging the thermodynamic energy equation (3.3) and using the hydrostatic relation $T \sim -\partial\Psi/\partial p$ to yield

$$\frac{\partial\overline{T}_2}{\partial t} = -\delta\frac{\partial}{\partial y}\overline{(v_2'T_2')} + 2\sigma_0\overline{\omega}_2 + 2h''(T^\dagger - \overline{T}_2). \quad (3.4)$$

We are interested in the dynamics at large meridional scales and the effect on the temperature gradient across the channel, defined by $\Delta\overline{T} \equiv \overline{T}_2|_{y=0} - \overline{T}_2|_{y=\pi}$. From (3.4) this can be approximated at equilibrium by

$$\Delta\overline{T}_{\text{eq}} \approx \Delta T^\dagger + \frac{\sigma_0}{h''}\Delta\overline{\omega}_2 - \frac{\delta}{2h''}\Delta\frac{\partial}{\partial y}(\overline{v_2'T_2'}), \quad (3.5)$$

where the last term is the differential eddy heat flux convergence or ''heat transport.'' We will vary the magnitude of the radiative equilibrium forcing $\Delta T^\dagger$ and measure the resultant $\Delta\overline{T}_{\text{eq}}$ and the resultant heat transport by various waves.[6] The contribution by the vertical velocity was small in all cases we studied.

Figure 5 shows output from model simulations. For a wide range of forcings, the solid line gives the total heat transport by all waves at equilibrium, and a cross the resultant temperature gradient. For very low forcings there is zero heat transport and, thus, the temperature gradient equals that of the Hadley solution (dashed line). When the forcing rises above the minimum critical temperature gradient, given in Fig. 4 as $\Delta\overline{T}_{\text{cr}} \approx 9$ K, the heat transport becomes nonnegligible. From this point higher, the total heat transport rises linearly with forcing, while the temperature equilibrates at a gradient that is lower than the Hadley solution's and fairly constant, even as the forcing is varied by an order of magnitude. This corroborates the first main premise of the nonlinear baroclinic adjustment mechanism listed in the introduction.

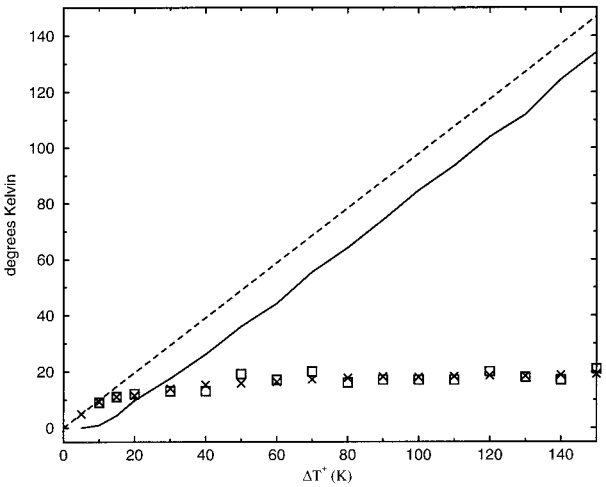

FIG. 5. Equilibrium temperature gradients (crosses) for a range of forcing for $\delta = 0.28$. Also shown is the radiative equilibrium Hadley solution (dashed line). Critical gradients from a linear stability analysis of the dominant heat-transporting wave in the equilibrated flow are given by the squares. The solid line is the total heat flux by all waves, $(\delta/2h'')\Delta\partial(\overline{v_2'T_2'})/\partial y$.

Figure 6 shows the heat transport by each wave separately at equilibrium over the same range of forcings. At low forcings (but above the Hadley solution) the most unstable wave $m = 11$ transports all of the heat. At a forcing near 15 K, however, this wave's contribution flattens out and other waves ($m = 10$ and 9) begin to transport significant heat. Notice that wavenumber 10 starts growing not when it becomes linearly unstable ($\Delta T^\dagger \approx 10$ K from Fig. 4) but rather when wavenumber 11 saturates. This agrees with the idea of a *nonlinear* mechanism to select the dominant wavenumber; a simple linear theory based on stability analysis would not be in accord with the results here. At a slightly higher forcing of $\Delta T^\dagger \approx 18$ K, $m = 10$ takes over dominance until, at $\Delta T^\dagger \approx 40$ K, it reaches *its* saturation level and dominance passes to wavenumber 9. The cascade continues to longer and longer scales as the forcing is raised.

Thus we confirm the upscale cascade theorized in section 2 above. Figure 6 also demonstrates the nonlinear wave thresholds directly. For $100 \leq \Delta T^\dagger \leq 150$ K, wavenumbers 8–11 each have a heat transport that does not rise much with the forcing, indicating that these scales have reached saturation and have passed energy to the longer scale waves, which dominate at these forc-

[6] As in Welch and Tung (1998), heat transports are approximated in the figures by the projection of $-\delta/2h''\partial(\overline{v_m'T_m'})/\partial y$ onto the cosy mode. They are in units of K and not K s^{-1} due to division by h''.

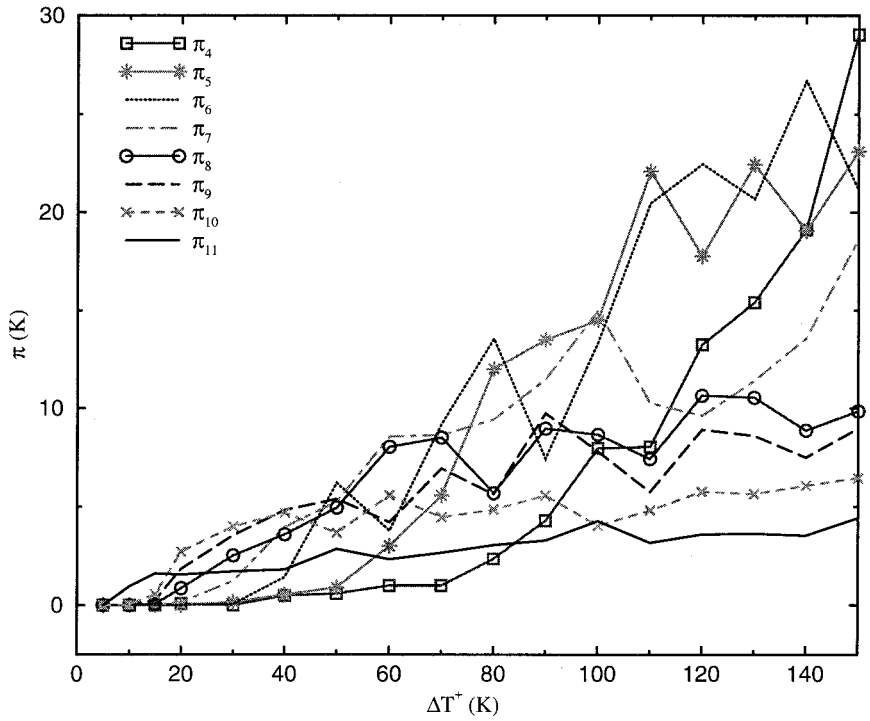

FIG. 6. Differential heat flux convergences, $(\delta/2h'')\Delta\partial(\overline{v_2'T_2'})/\partial y$, projected onto the cos$y$ mode, at equilibrium vs forcing for $\delta = 0.28$. Legend indicates wavenumbers. Only waves with non-negligible heat transport are included. (This is the same data as in Fig. 9 but plotted differently.)

ings. Furthermore, the saturation level for the shorter waves are lower than for the longer waves:

$$(\Pi_{11})_{\text{satn}} < (\Pi_{10})_{\text{satn}} < (\Pi_9)_{\text{satn}} < (\Pi_8)_{\text{satn}},$$

which agrees with the relation (2.13).

To investigate the nature of the equilibration, a linear stability analysis has been performed on the zonal mean state of the flow *at equilibrium* for each forcing. From Fig. 6, the dominant heat transporting wave can be identified for each equilibrium, and the critical gradient determined for that wave in the equilibrated flow. These values have been plotted on Fig. 5 as squares. That the critical temperature gradients (crosses) lie near or on the critical gradient of the dominant heat transporting waves at equilibrium (squares) agrees with the conceptual model of nonlinear baroclinic adjustment presented in Fig. 2 above. The flow has been made approximately neutral with respect to the dominant wave, implying that this wave acts in a quasi-linear fashion [as envisioned by Stone (1978) for the most unstable wave]. In the process, all longer waves have been rendered linearly stable. This can be seen from the marginal stability curve for the *equilibrated* flow at $\Delta T^{\dagger} = 90$ K (solid line) in Fig. 4. Wavenumber 5 is the longest wave to transport heat in this case (as given by Fig. 6), and it reduces $\Delta\overline{T}$ down to near its critical gradient, $\Delta\overline{T}_{\text{cr},5}$, rendering itself approximately neutral. As this is lower than the critical gradient for longer waves, wavenumbers $m = 1 - 4$ are linearly stabilized as well.

The process of wave breaking also can be demonstrated with model output. Figure 7 shows various snapshots in time of a model run at $\Delta T^{\dagger} = 120$ K. Each frame shows contours of upper-layer PV versus x and y at a point in time in the evolution to equilibrium, with solid (dotted) contours indicating total PV greater (less) than the average planetary contribution, f_0. The run is started from the (perturbed) Hadley solution, which at this forcing is supercritical to wavenumbers 1–14 (Fig. 4, dashed curve). Early on at 1.2 days, the most unstable wave (wavenumber 11) is the primary perturbation to the PV contours, as can be seen from the number of peaks in the perturbed f_0-contour in panel a. This wave does not maintain dominance, however. As the evolution proceeds, the dominant wave observed becomes longer and longer: from $m = 11$ initially to $m = 10$ (not shown) to $m \approx 9$ at 2.3 days (panel b) to $m \approx 8$ at 3.5 days (panel c), etc. Finally at equilibrium, it is $m \approx 6$ that is dominant, as shown at 92.6 days in panel d (and which agrees with Fig. 6).

Dominance shifts to a longer scale when the PV contours of the currently dominating wave curl up such that regions of negative PV gradient are created. Initially the gradients are dominated by β_0 and hence are everywhere positive, as in panel a. Waves then begin to grow, distorting the contours. If a wave becomes very large, long

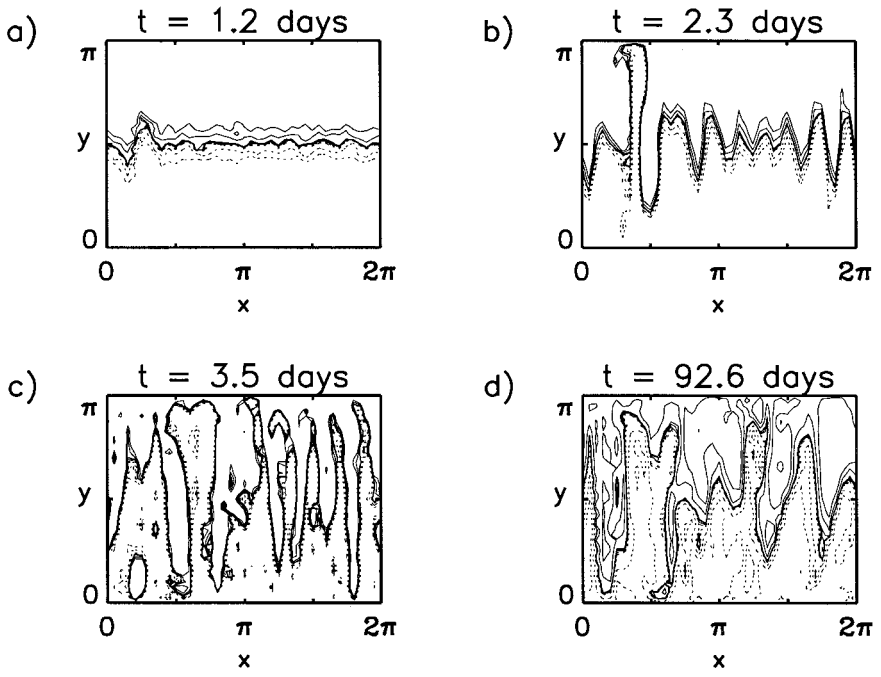

FIG. 7. Contour maps over time of potential vorticity in the upper layer vs x and y for $\Delta T^{\dagger} = 120$ K. Thick solid line is the f_0 contour; thin solid and broken lines indicate $Q_1 > f_0$ and $Q_1 < f_0$, respectively. (The contour interval is not constant but rather has been chosen to demonstrate most clearly the process of wave breaking.)

thin fingers of PV start to form, as in panel b for wavenumber 9. Eventually these fingers begin to curl over onto themselves, creating regions of negative PV gradient; for example, see the top left section of panel b or the top of panel c. Where this occurs, small-scale instabilities begin to grow. Panel c shows PV fingers that curl over and are being ''pinched off'' by instabilities that have arisen on the side(s). Small ''blobs'' of PV thus are created, and these are in turn broken up, as they have negative PV gradients due to their closed contours. The blobs become smaller and smaller until they are dissipated by (subgrid) friction. In this way, further growth of wavenumber 8 in panel c is prevented. The next longer wave begins to emerge in the PV contours as it grows larger than the breaking wave.

Another demonstration of the generalized Charney–Stern theorem specifically addresses (2.1). From this relation we expect that each saturated wave will have yielded a Q'_y that is about equal in magnitude to $\overline{Q}_y$. This is demonstrated by Fig. 8, which shows the upper-level wavy and zonal mean PV gradients over time for $\Delta T^{\dagger} = 100$ K. The top panel is for values at $y = \pi/2$ and shows the initial evolution from the Hadley state. At a short time of $t \approx 40$ (about 5 days) several waves grow to large amplitude because they are baroclinically unstable, and hence their $|Q'_{1,y}|$ grow large as well. These waves extract energy from the mean flow, reducing the cross-channel temperature gradient and hence $\overline{Q}_{1,y}$ by relation (2.4).[7] In the process, at some point $|Q'_{1,y}| > \overline{Q}_{1,y}$, and thus the breaking criterion of Garcia is satisfied and the waves break. A series of peaks in wavy PV gradient occurs in Fig. 8 for the different waves, and each PV gradient then successively falls. This reduction of the wave amplitudes allows the temperature gradient and thus $\overline{Q}_{1,y}$ to increase, bringing the wavy and zonal mean PV gradients back into approximate equality. In the long run, the waves maintain an amplitude such that $|Q'_{1,y}| \approx \overline{Q}_{1,y}$ for the saturated modes at equilibrium. This is shown in the lower panel for later times and a different latitude within the channel. (Both panels are similar at other values of y.)

Finally, we consider spectra of heat flux and energy from model output. Figure 9 shows the same data as in Fig. 6, but it has been rearranged so that each curve corresponds to a single forcing, giving the transient heat transport by each zonal wave at equilibrium. Also on this log–log chart are thin lines of constant slope -3 to -4. It can be seen that overall the model spectra do vary approximately as m^{-4}. This graph shows evidence of the saturation thresholds discussed in the previous section. Notice how, as the forcing is raised, the spectra

[7] Note that $\partial\overline{T}/\partial y < 0$, but this gradient generally decreases in magnitude with height in the upper troposphere such that $\partial/\partial z\,(\partial\overline{T}/\partial y) > 0$ at level 1. Thus decreasing the *magnitude* of $\partial\overline{T}/\partial y$ in (2.4) also decreases its vertical gradient and hence $\overline{Q}_{1,y}$.

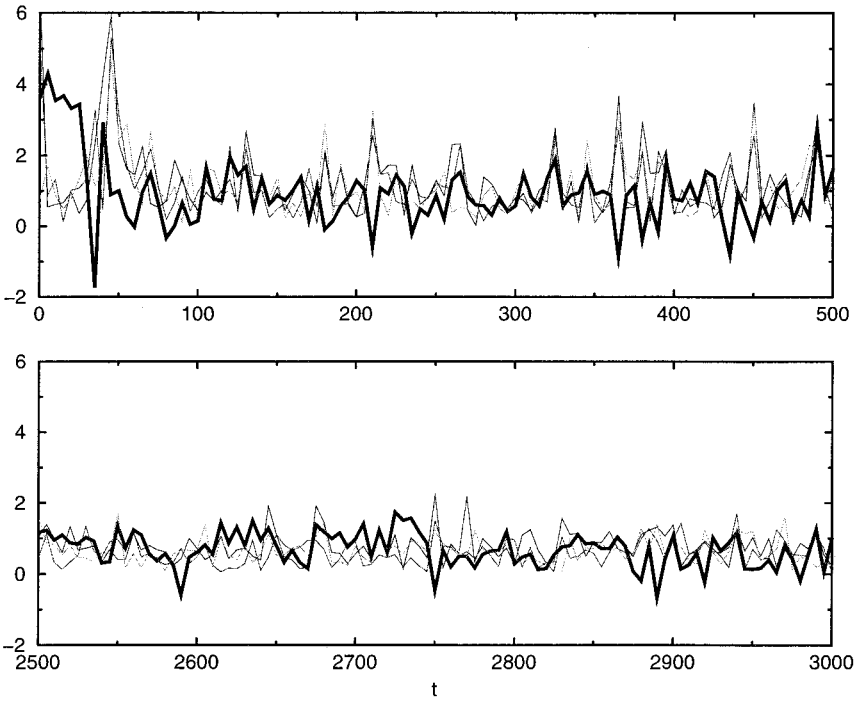

FIG. 8. Meridional gradients of potential vorticity vs time at the upper level: $\overline{Q}_{1,y}$ (heavy dark line) and $|Q'_{1,y}|$ for zonal wavenumbers $m = 5, 7, 9, 11$ (thin solid lines). Top panel is at $y = \pi/2$ starting at $t = 0$, and bottom at $y = \pi/3$ for later times.

in the heat transporting range asymptotically approach an enveloping curve, roughly given by the curve for the highest forcing plotted ($\Delta T^{\dagger} = 140$ K). This envelope is the locus of saturation levels for each wavelength.

Figure 9 also shows the wave that dominates the heat transport moving to a longer and longer scale as the forcing is raised. For example, as the forcing changes from $\Delta T^{\dagger} = 60$ K (a proxy for summer; dashed line) to 80 K (proxy for winter; line with circles), the dominant heat transporting wave in the model shifts from $m = 7$ to $m = 6$. A similar shift occurs in the real observations in Fig. 1; in the Southern Hemisphere the dominant wavenumber moves from 6 to 5, summer to winter. Interestingly, this sort of shift does not occur in the model if we raise the forcing yet higher. Figure 9 shows that, even for forcing levels about twice that in our current climate, the dominant wave remains $m \approx 6$. This is because wavenumber 6, by (2.13), has a high nonlinear threshold that has not yet been reached by $\Delta T^{\dagger} = 140$ K. Thus the theory of nonlinear baroclinic adjustment not only allows us to understand observations, but also to make predictions, as in the following. If the effective solar forcing were to increase from the current value, the impact on the heat flux spectrum would be small. The amount of heat transport by synoptic-scale waves $m \geq 7$ would remain at their saturated values, and the dominance by wavenumber 6 would continue. Only the amount of heat transport by this dominant wave would change, increasing linearly with the forcing to maintain the same overall robust temperature gradient.

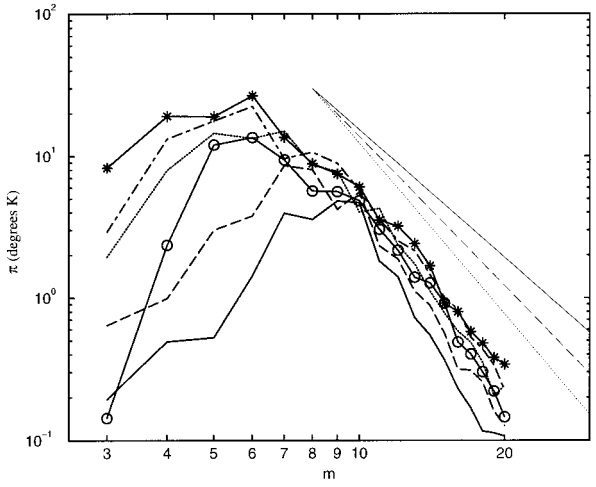

FIG. 9. Spectra of transient eddy heat flux for various forcings in model simulations: $\Delta T^{\dagger} = 40$ K (solid), 60 K (dashed), 80 K (solid with circles), 100 K (dotted), 120 K (dot–dashed), and 140 K (solid with stars). For each point, the heat flux convergence, $-(\delta/2h'')\partial(\overline{v'_m T'_m})/\partial y$, has been projected onto the cos$y$ mode. (This is the same data as in Fig. 6 but plotted differently.) Thin lines as in Fig. 1.

Let us now consider the spectrum of transient energy. First we show with model results that it has similar features to the heat transport spectra above. In Table 1 we compare the synoptic wavenumber of maximum per-

TABLE 1. The zonal wavenumbers of maximum perturbation energy (in the synoptic range) and maximum transient heat flux convergence. All calculations are at equilibrium.

$\Delta T\dagger$ (K)	$(m_{\text{maxE}})_{\text{syn}}$	m_{maxII}
20	10	10
50	7	6
80	5	6
110	5	5
140	4	6

turbation energy (departure from the time and zonal mean) with that of maximum heat flux convergence (taken from Fig. 6) for various forcings in the two-level model. It can be seen that the wavenumbers are very close at all forcings. There is indeed a difference between the dominant heat-transporting mode and the synoptic-scale mode with maximum perturbation energy. First, the wave of maximum energy is not necessarily the wave of maximum energy *extraction* from the mean flow. Model simulations here and in other studies do show them to be close, however (Larichev and Held 1995). The wave of maximum energy often is just slightly longer than that of highest extraction, seemingly a by-product of the continual cascade of energy to longer waves, as also found in Fig. 9 of Haidvogel and Held (1980). Further, the wave of maximum energy extraction is not the same as the wave of maximum heat transport. However, both are quasi-linear quantities, measuring interaction between a wave and the mean flow, and model simulations show that these two scales are also close. Thus one would expect that the (synoptic) wavelength of maximum energy and that of maximum heat transport would be similar. This similarity implies that nonlinear baroclinic adjustment should be able to explain the occurrence of a synoptic-scale peak in the energy spectrum as well as in the heat flux spectrum.

Now look at the shape of the energy spectrum for synoptic-scale waves, as shown in Fig. 10 for several different forcings. Note that there is again an enveloping of the spectra as the forcing is raised, as with the heat flux in Fig. 9. Comparing against the thin lines of constant slope, it can be seen that the energy decays at a rate similar to that of the heat flux. However, here most of the curves are closer in slope to -3 or -3.5 than to -4, while the opposite was true in Figs. 9 and 1. This agrees with the prediction (2.16). Therefore, the nonlinear baroclinic adjustment theory delineated above can also explain the synoptic peak and shape of the transient energy spectrum over a range of forcings.

We note that Fig. 10 shows a long-wave maximum of energy as well as a synoptic wave maximum at each forcing in model simulations. This is true of the heat flux convergence as well. (Fig. 9 hides this fact because its values are all projections onto cos$y$, whereas the long-wave maximum usually occurs at a shorter meridional scale.) There is some evidence of a long-wave peak of

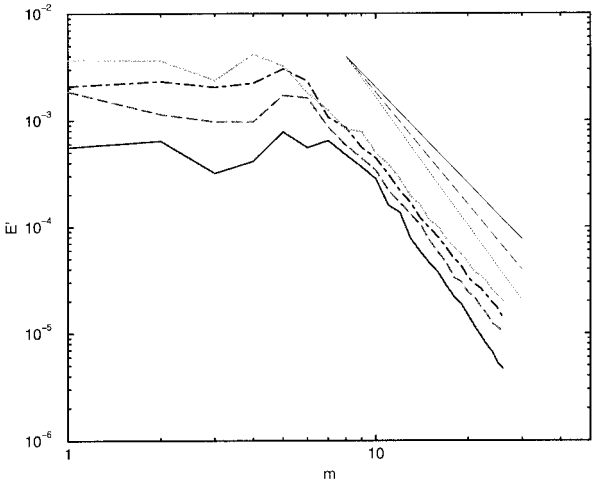

FIG. 10. Perturbation energy spectra at equilibrium. Solid line is for $\Delta T^{\dagger} = 50$ K, dashed line for 80 K, dot–dashed line for 110 K, and dotted for 140 K. Thin lines as in Fig. 1.

transient energy in the real atmosphere, due to large available potential energy at planetary scales (Willson 1975, Fig. 5; Tanaka and Kung 1988, Figs. 5 and 6). However, in this work we are concerned with the synoptic part of the spectrum and will not further investigate the long waves (except in the discussion of Rhines' theory in section 4).

c. Observations of heat flux

Let us also test our theory against observed heat flux spectra in the real atmosphere. Figure 1 shows observations of heat flux, $\overline{v'_m T'_m}$, at 47° and 700 mb for each zonal wave in four different season/hemisphere pairs (Randel and Held 1991). The Southern Hemisphere data provide the most direct comparison to our model, which has no topography. These curves show the same enveloping described above, and the heat transporting waves vary with zonal wavenumber roughly as m^{-4}. Therefore, the nonlinear baroclinic adjustment theory's prediction for the shape of the heat flux spectrum agrees with both model simulations and observations of the real atmosphere.

d. Model validation

In order to use the model to corroborate the theory, as we have done in section 3b above, we should compare model simulations with observed data to confirm the model's validity. First, we recognize that the static stability varies between the seasons, and thus more specific values of σ_0 have been calculated for winter and summer separately, using data from Peixoto and Oort (1992). From their Fig. 7.5, and with $\rho = \rho_4 e^{-z/H}$ with $H \approx 7$ km and $\rho_4 \approx 1.275$ kg m^{-3} from Wallace and Hobbs (1977), we determine the following values for nondimensional σ_0:

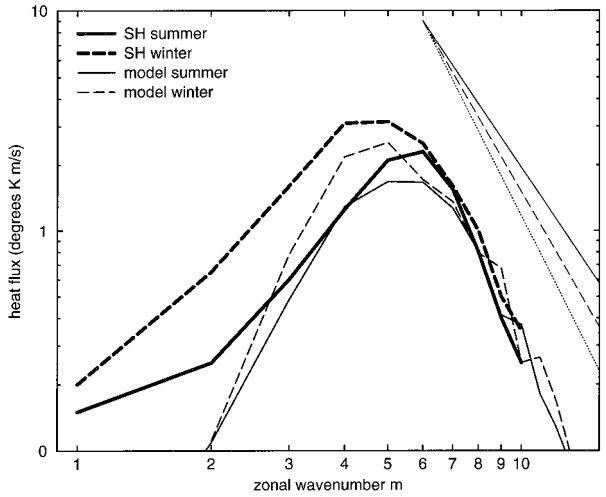

FIG. 11. Transient heat flux $\overline{v'T'}$ at 47°S and 700 mb from Randel and Held (1991) for two seasons (thick curves), as in Fig. 1. Thin curves are from model simulations of $\overline{v'T'}$ at 50° and 600 mb for summer (solid) and winter (dashed). See text for details. Thin straight lines as in Fig. 1.

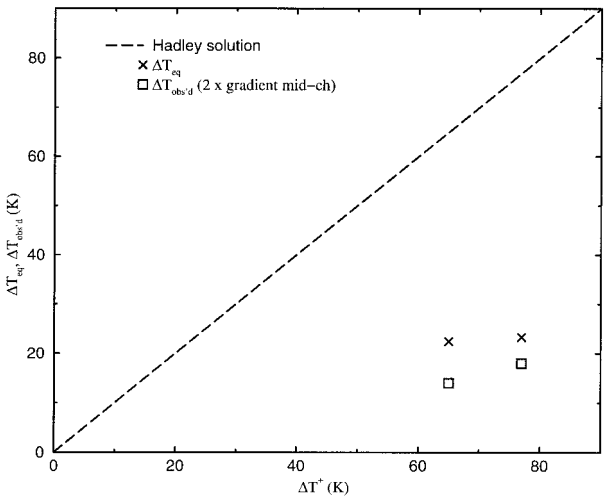

FIG. 12. Equilibrated temperature gradients: the dashed line is the Hadley solution, crosses are the results of model simulations, and boxes are from observations. See text for details.

$$(\sigma_0)_{\text{winter}} \approx 0.085$$

$$(\sigma_0)_{\text{summer}} \approx 0.077. \tag{3.6}$$

We also choose the magnitude of forcing for each season separately, as:

$$(\Delta T^{\dagger})_{\text{winter}} \approx 77 \text{ K}$$

$$(\Delta T^{\dagger})_{\text{summer}} \approx 65 \text{ K}. \tag{3.7}$$

These forcings are in the same ratio, winter to summer, as the net radiation at the top of the atmosphere (from Peixoto and Oort 1992, Fig. 6.14d). Finally, for comparing with observations we have used an 18-day timescale for the Newtonian cooling parameter h''. (In all other parts of this work, the model uses a slower value of 56 days for h'', in order to elucidate the dynamics.)

Two different comparisons were made. Figure 11 shows heat flux spectra from observations of winter and summer in the Southern Hemisphere, as in Fig. 1. The new graph includes spectra from winter and summer model simulations as well, with parameter values noted above.[8] The magnitude of the model-simulated heat flux is very near in magnitude to that of the real atmosphere, for both seasons and all heat transporting waves. In particular, the short-wave ends of the modeled spectra fall right on top of the observed, showing approximately the same slope. Also, the peak of the modeled summer spectrum is at $m \approx 6$, shifting to $m = 5$ in the winter. This duplicates the shift that has already been mentioned in the real data. Notice also that the model results show no difference in heat flux in the shorter waves season to season, which is the same as in the observations and which was explained by the saturation mechanism in the baroclinic adjustment theory. One discrepancy between the model and the real atmosphere is in the long waves: they have smaller amplitude in the former than in the latter. This is presumably due to the absence of any forcing mechanisms other than baroclinic instability in the model. In the real atmosphere many processes exist that can generate nonstationary long waves, among them topography and other longitudinally asymmetric forcings such as diabatic heating. By omitting such influences from our model, we reduce the amplitude and heat transport possible by long waves.

We also consider temperature gradients produced by the same two model runs; these are shown as crosses in Fig. 12. They are compared against observed values (squares) of the temperature gradient in midchannel; that is, $-2\partial\overline{T}_{\text{obs}}/\partial\hat{y}$ at $\hat{y} = \pi/2$ (Peixoto and Oort 1992, Fig. 7.5). Figure 12 shows that the results of the model are strikingly close to the observations. First, the model has approximated well the large reduction of the temperature gradient from the radiative equilibrium value, given by the dashed line. Second, the model and observed values are fairly robust in spite of large differences in seasonal forcing, agreeing with Stone (1978). Finally, the model results show a slight rise in equilibrium gradient from summer to winter. This meets with our expectations and agrees qualitatively with the observations. The difference between winter and summer in the real atmosphere is larger than what the model predicts, but given that the model results are projected onto cos$y$ and are the result of many simplifications, such a discrepancy is not surprising or alarming.

Therefore we have some evidence that our model,

[8] The output of the model has been translated, from the projection of the heat flux convergence onto the cos$y$ mode, to the heat flux at midchannel, which is approximately the measure used by Randel and Held (1991).

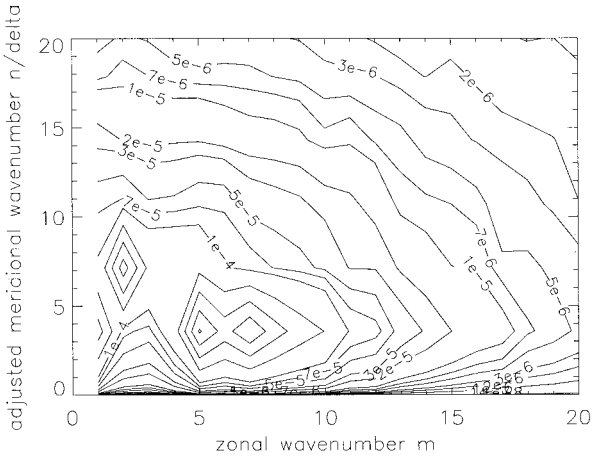

FIG. 13. Perturbation energy vs zonal wavenumber m (abscissa) and adjusted meridional wavenumber n/δ (ordinate) at equilibrium for $\Delta T^{\dagger} = 50$ K. The contour interval is not constant for $E \leq 1e-4$ (and hence is labeled), and for $E > 1e-4$ it is constant at $1e-4$.

albeit a simple two-level quasigeostrophic model in a beta-plane channel, has relevance to the real atmosphere. Hence we expect that the mechanism of nonlinear baroclinic adjustment, which the model demonstrates, is similarly meaningful.

4. Relation to other theories

Several theories have been proposed by other authors to explain various aspects of the equilibration of baroclinic flows. Let us consider the argument given by Rhines (1975) for the wavenumber of maximum energy. He developed a formula based on geostrophic turbulence arguments for the wave scale that would dominate in a flow subject to both turbulence and Rossby wave dynamics. This is relevant to our present parameter regime. Rhines reasoned that nonlinear triad interactions among short waves would result in a reverse cascade of energy upscale (Charney 1971), but that such interactions would diminish at the large scales, which are dominated by the linear dynamics of Rossby waves due to the large Coriolis force. Thus the upscale cascade would terminate at some wavenumber for which the Coriolis force and the nonlinear terms have the same magnitude. Rhines calculated this wavenumber of cascade arrest as $k_\beta \equiv (\beta/U_{\rm rms})^{1/2}$, where k_β is a total (two-dimensional) wavenumber and $U_{\rm rms} = (u^2 + v^2)^{1/2}$ is the magnitude of the root-mean-square eddy velocity. This can be expressed for our study as

$$\left(m^2 + \frac{n^2}{\delta^2}\right)_\beta \equiv \frac{1}{\delta}\sqrt{\frac{\beta}{U_{\rm rms}}} \qquad (4.1)$$

(all quantities are nondimensional).

To test whether the Rhines wavenumber of cascade arrest accords with our energy maximum, we must consider energy versus total horizontal wavenumber, not just zonal wavenumber. Therefore we have plotted in Fig. 13 the perturbation energy versus both zonal and meridional wavenumber for $\Delta T^{\dagger} = 50$ K at equilibrium. The meridional wavenumber n has been adjusted so that equal distances along the abscissa and ordinate represent equal dimensional wavelengths. The Rhines theory predicts that energy would be a maximum in a circular arc around the origin and that the radius of this arc would be that given by (4.1). For the moderate forcing of Fig. 13 we see two regions of maximum energy: one at synoptic scales of $m = 5$–7, $n = 1$ ($n/\delta \approx 3.6$) and the other a long wave at $m = 2$, $n = 2$ ($n/\delta \approx 7.1$). These two maxima are at approximately the same distance from the origin, that is, have the same total (dimensionless) wavenumber $(m^2 + (n/\delta)^2)^{1/2} \approx 6$–$7$. Thus it is possible that the two extrema are just different orientations of the same isotropic maximum. (Because the meridional wavenumber n can take only integral values, the energy is quantized in that dimension and thus the maximum arc is broken up into distinct peaks, but its underlying circular nature can still be deduced.) Note also that the contours of energy for shorter waves form roughly circular arcs centered at the origin.

TABLE 2. Rhines total wavenumber, $(m^2 + n^2/\delta^2)_\beta$, for various forcings as calculated from the rms eddy velocity, $U_{\rm rms}$, according to (4.1). The synoptic wavenumber of maximum perturbation energy from model runs, $(m^2 + n^2/\delta^2)^{1/2}_{\rm Emax}$, is also included. All calculations are at equilibrium.

$\Delta T\dagger$	$U_{\rm rms}$	$(m^2 + n^2/\delta^2)_\beta$	$(m^2 + n^2/\delta^2)^{1/2}_{\rm Emax}$
20	0.04	8.0	10.6
50	0.11	4.8	6.1
80	0.16	4.0	6.1
110	0.21	3.5	6.1
140	0.24	3.3	5.3

Therefore, could we explain the presence of the *two* peaks of energy in each curve in Fig. 10 by Rhines' theory? The answer appears to be no. The quasi-isotropy in Fig. 13 is not found consistently at other forcings. At low $\Delta T^{\dagger}$, the maxima of energy are sufficiently weak that a two-dimensional plot of energy has no clear structure. As the forcing is raised to high values, the two maxima seen for $\Delta T^{\dagger} = 50$ K both move in toward the origin, but not uniformly so, and thus the circular ''Rhines ring'' is lost. For all forcings the energy at the longest scales is distinctly anisotropic. In addition, investigations into the energetics of the evolution to equilibrium at various forcings show a nonlinear cascade that does not always flow to, and only to, the isotropic Rhines total wavenumber. This is not really surprising, given the difference between our model and Rhines' assumptions. (See below.) Thus, in its strict two-dimensional sense the Rhines mechanism does not seem to be operating here.

However, as we are interested primarily in the synoptic heat transporting waves, let us see if the Rhines mechanism can explain the *synoptic* energy maximum. In Table 2 Rhines' total wavenumber is compared

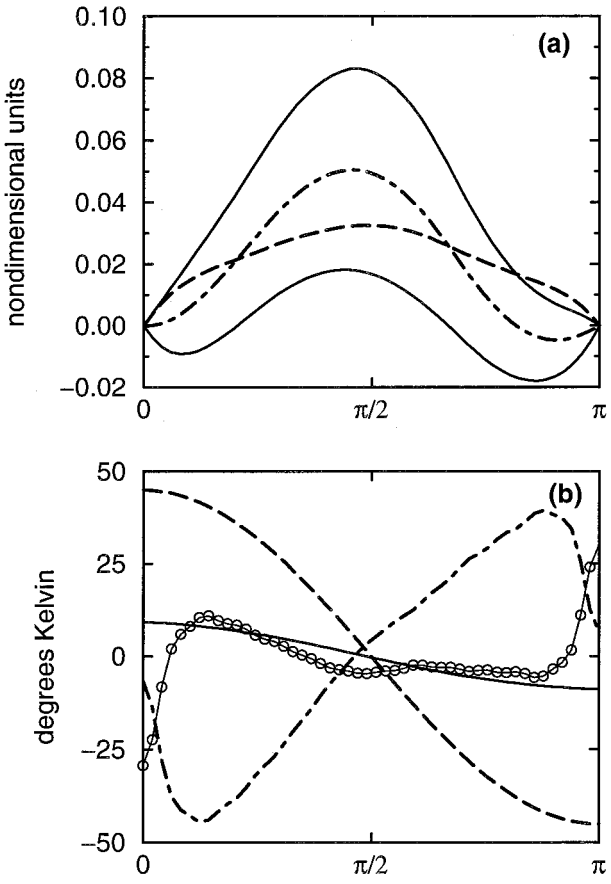

FIG. 14. Equilibrium for $\Delta T\dagger = 90$ K. Panel (a) shows zonal mean zonal velocities: solid lines are $\overline{u}_1$ (upper) and $\overline{u}_3$ (lower); dashed line is baroclinic velocity $\overline{u}_{\rm BC} = \frac{1}{2}(\overline{u}_1 - \overline{u}_3)$ and dot-dashed is barotropic velocity $\overline{u}_{\rm BT} = \frac{1}{2}(\overline{u}_1 + \overline{u}_3)$. Panel (b) shows components of zonal mean thermodynamic energy equation (3.4): radiative equilibrium temperature $T\dagger$ (dashed line), heat flux convergence $-(\delta/2h'')\partial(\overline{v_2'T_2'})/\partial y$ (dot–dashed line), vertical velocity $(\sigma_0/h'')\overline{\omega}_2$ (circles), and resultant equilibrium temperature $\overline{T}_{2,\rm eq}$ (solid line).

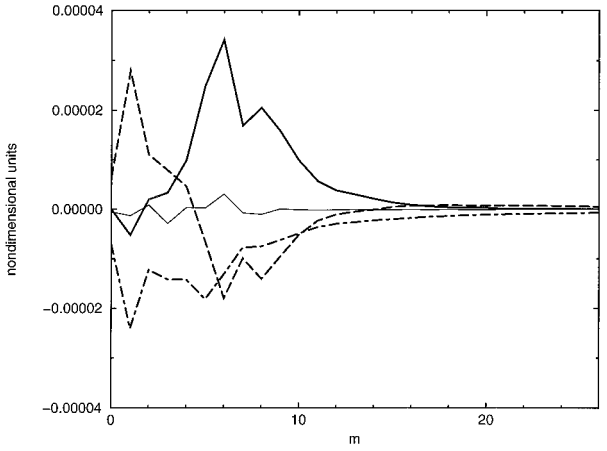

FIG. 15. Components of perturbation energy growth rate at equilibrium for $\Delta T^{\dagger} = 90$ K: quasi-linear extraction from the mean flow (solid line), nonlinear transfer (dashed line), and dissipation plus forcing (dot–dashed line). The thin solid line is the total rate of change of energy in each mode.

against the total *synoptic* wavenumber of maximum energy for various forcings. In each case $U_{\rm rms}$ is time- and channel-averaged at equilibrium; thus it is a measure of the barotropic energy in the channel, as in the study by Haidvogel and Held (1980).

It can be seen that Rhines' wavenumber is indeed a proxy for the synoptic scale of maximum energy. Furthermore, there is nonlinear flow to this synoptic wave during the evolution to equilibrium, as Rhines' theory predicts. We do note that in all cases his wavenumber is smaller than the actual dominant wavenumber, a feature found by Whitaker and Barcilon (1995) as well. There could be a number of reasons for this. First, we must recognize that the Rhines calculation is based on a simple balance of terms and hence is intended as a ball park figure, not a precise prediction. Second, Rhines' theory neglects viscosity and thermal forcing. These both act as damping on the waves, and such a drain of energy from the cascade has been thought to prevent it from reaching as far upscale as it would without the damping (Panetta 1993; Lilly 1972). Thus, a viscous k_β would be larger than the prediction of (4.1) and likely more in agreement with the simulation results.

Another possible reason for the difference is that Rhines' ideas were developed for a fluid in a state of homogeneous isotropic turbulence, whereas our model has intentionally been run in a parameter regime, that is more like the real atmosphere: a channel that is not infinitely wide and throughout which the eddies *can* change the mean flow. In studies with models forced to be homogeneous (Haidvogel and Held 1980; Panetta 1993; Pavan and Held 1996), the isotropic results are indeed found to match with the Rhines theory. Here our simulations are clearly less isotropic. Thus Rhines' assumptions do not really match with our situation, and it is not not surprising that his wavenumber of cascade arrest cannot explain all of our energetics. However, his theory does seem to explain the dynamics of the synoptic wave of maximum energy and can roughly determine its scale.

Our nonlinear baroclinic adjustment theory also accords with the wave–wave equilibration theory of Salmon (1980) in his study of quasigeostrophic turbulence. This can be seen in Fig. 15, which shows the perturbation energy growth, and components thereof, for each zonal mode at equilibrium for a winterlike forcing of $\Delta T^{\dagger} = 90$ K. [Calculations follow the method of Whitaker and Barcilon (1995).] The solid line represents quasi-linear extraction of energy from the mean flow, the dashed is nonlinear energy transfer between waves, and the dot–dashed line is the total of the linear processes: Ekman friction, subgrid damping, and Newtonian cooling. Note that the components of energy change sum to approximately zero in our time average, as indicated by the thin solid line, proof that the system is indeed at equilibrium.

The figure shows that there is nonlinear transfer of energy out of wavenumbers 5–12, whereas wavenumbers 1–4 gain energy nonlinearly. That is, the most unstable waves lose energy to longer, less unstable waves. This is due to the fact that these shorter heat transporting waves have reached their saturation levels and are breaking, as described above, and their energy is taken up always by waves of longer scale due to the relation (2.13). Figure 15 also shows that the longer waves are losing energy to dissipation. Because the most unstable waves continually lose energy nonlinearly, they can be maintained in a state in which they are linearly unstable. This is confirmed by the marginal stability curve at equilibrium for the case $\Delta T^{\dagger} = 90$ K in Fig. 4 (solid line). The mean flow is supercritical to the most unstable waves at equilibrium. (We note that the results in our Fig. 15 are very similar to those of Whitaker and Barcilon (1995); cf. their Figs. 7 and 9.)

The above energetics fit with Salmon's wave–wave equilibration theory, which he developed to explain equilibration in a fluid with a forced mean baroclinic state, including Ekman friction at the earth's surface (Salmon 1980). An equilibrium is achieved in which the most unstable waves gain energy quasi-linearly from the forcing (i.e., from the mean flow) and lose it nonlinearly to longer, less unstable waves on which dissipation acts. With such an energy balance, an equilibrium that is ''supercritical'' relative to the most unstable waves is possible.

We can summarize the main elements of the dynamics displayed in Fig. 15 by dividing all zonal wavenumbers into two groups. Wavenumbers 1–4 in net gain energy from the mean flow, but not as much as $m \geq 5$. Wavenumbers 1–4 gain energy nonlinearly, while $m \geq 5$ lose energy. Finally, the longer waves lose more energy to forcing and damping than the shorter waves. It is now apparent that this is exactly the dynamics studied in Welch and Tung (1998), in which only two waves were unstable. In that case all the dynamics was compressed into the only two active waves: the longer wave $m = 1$ played the role of the long-wave group here (wavenumbers 1–4) and the short-wave $m = 2$ played the role of the shorter waves $m \geq 5$. (See their Fig. 6T.)

Thus Salmon's theory can successfully describe the equilibrium dynamics of our baroclinic model in disparate parts of parameter space, and our theory agrees with his in this sense. We note that nonlinear baroclinic adjustment goes a step further, giving the dynamic mechanism for each wave and explaining how the waves interact over time to yield the final equilibrium state.

As an aside we note that there is some stabilization of the flow due to the barotropic governor effect (James 1987). This can be seen from Fig. 14a, which shows the zonal mean zonal velocities at equilibrium for the case $\Delta T^{\dagger} = 90$ K. The barotropic velocity u_{BT} (dot-dashed line) is slightly larger in magnitude than the baroclinic flow u_{BC} (dashed line), and the former has somewhat of a barotropic shear as well. These two features suggest a lessening of the baroclinic instability of the flow by the James barotropic governor mechanism. Figure 4 shows the result of this effect: the marginal stability curve for the equilibrated flow (solid curve) is higher than that for the initial Hadley flow (dashed curve). (Note that the stability analysis performed incorporates the meridional profile of the flow being analyzed; hence it includes any barotropic governor effect automatically.) The influence of the barotropic governor is not dominant, however, in that the flow at equilibrium is still unstable to the smaller-scale synoptic waves.

Yet another explanation of baroclinic equilibration has been espoused by Farrell and collaborators (Farrell and Ioannou 1994; DelSole and Farrell 1995; Farrell and Ioannou 1995; DelSole and Farrell 1996). In the studies listed, the authors used *linearized* quasigeostrophic equations and showed how the nonnormality of the linear operator can lead to transient growth of nonmodal waves. Starting with a single initial value problem, Farrell (1989) demonstrated that an optimal perturbation to the mean atmosphere in such a system can mimic the development of a single midlatitude cyclone. He reasoned that the combined effects of many cyclones, that is, the effect of baroclinic instability on climate, then can be simulated by continuously forcing the linearized system. This was done by modeling the omitted nonlinear interactions as a stochastic forcing in all wavelengths (plus a linear dissipation). Using this technique, the above authors were able to generate the eddy variance, that is, heat and momentum fluxes, among other features observed on synoptic scales in the real atmosphere. They argued, therefore, that it is transient growth due to nonnormality of the linearized operator that we observe as baroclinic phenomena.

In this study we have not made any assumption concerning the modal structure of the solution. Our calculations were done by stepping the fully nonlinear equations forward in time, allowing many waves to interact with each other and with the mean flow. Thus both normal modes and nonmodal waves are allowed. That our results can be explained with only normal mode thinking may be an issue of the function of nonlinearities, as we now discuss.

In a linearized problem for which the operator possesses normal modes but is nonnormal, transient growth at small times gives way to normal mode (exponential) growth or decay at later times. This has been demonstrated by Farrell (1982) for the most unstable wave in the Eady problem. (See his Fig. 4.) Farrell and colleagues' nonnormal linear theory of statistical baroclinic equilibration assumes that the system never proceeds past the transient stage to see the effects of growing (or decaying) normal modes. Energy is scattered by nonlinearities (parameterized as stochastic forcing), preventing evolution to an equilibrium state. On the other hand, our calculation of nonlinear clinic adjustment allows for short-term transiency, but it does not require that the system remain in this linear phase. The flow in

our simulations evolves past the transient stage into a nonlinear regime, wherein the amplitudes of the normal modes are kept in check by nonlinear interactions among waves. The discussion of section 2 is particularly simple because the nonnormal growth does not alter the mean flow significantly in our case; hence normal modes of the original wave-free state are similar to those of the final state.

A key difference between the nonnormal theory and ours, then, is the nonlinear interactions and the timescales over which they are presumed to have impact. Farrell and colleagues assume that nonlinearities act rapidly and catastrophically to scatter energy and interrupt the evolution to equilibrium. In this study we have made no such assumption, allowing the nonlinear interactions to occur at whatever pace the governing equations dictate. Our simple two-level simulations show nonlinearities acting in a different manner than Farrell's theory. Rather than stoking the nonnormal behavior, the nonlinear interactions here gradually overpower the transient growth and ultimately balance the (linear) growth of normal modes.

Whether the character of our nonlinearities is found in a more sophisticated model or in the real atmosphere is not yet known. A more detailed inspection of the observed wave–wave (and wave–mean) interactions in the real atmosphere, and a comparison thereof with the stochastic forcing suggested by Farrell and with our equilibrium dynamics, should be done. We point out that Farrell's theory is diagnostic and not prognostic, for one needs to know the equilibrated state in order to linearize the system about it, that is, to calculate the linear operator.

Finally, we note that Lindzen (1993, 1994) has proposed an alternative theory for the equilibration of baroclinic flows. He suggests a mechanism of neutralization, in which the atmosphere is continually striving for a state that is linearly neutral or stable to perturbations. That theory is clearly different from ours, for the former requires *all* waves to be linearly stable at equilibrium. Nonlinear baroclinic adjustment proposes that waves can be stabilized by different methods, in particular nonlinearly; not all waves must be linearly stabilized in order to achieve an equilibrium. This is evident in the marginal stability curve at equilibrium of Fig. 4 (dashed line); only the long waves have been linearly neutralized, while the short waves remain linearly unstable even at equilibrium. This was also found in the two-wave study of Welch and Tung (1998), and thus appears to be true over a wide range of parameter space.

5. Model issues

In this study we have chosen to use the simplest possible model that still allows for baroclinic dry dynamics to occur, neglecting more realistic features such as a variable static stability, topography and hence stationary waves, a spherical geometry, or moisture. Our goal has been to investigate and demonstrate in the clearest way the qualitative features of meridional heat transport. However, issues arise as to the consequences of some of our simplifications, which we must now address.

A model with only two levels in the vertical cannot properly simulate the real atmosphere. However, there is a correspondence between linear stability analysis of a two-level model and tropospheric observations: the critical gradient in the former corresponds to the cutoff in the atmosphere between shallow waves, ineffective at transporting heat, and long deep waves, which can efficiently flux heat poleward (Held 1978). Furthermore, it appears that adding more levels in the vertical may not change the qualitative results of the model. Pavan (1996) showed in her quasigeostrophic Boussinesq model that increasing the layers from 3 to 20 had little effect on the main features of the solution. High vertical resolution was needed for qualitative convergence only when eddy momentum flux was crucial, for example, in situations with a strong barotropic governor effect (James 1987).

We point out that the static stability has been held constant over time in this study. However, an important process in equilibrating baroclinic flows, in addition to the reduction of the horizontal temperature gradient, is the adjustment of the vertical temperature profile via vertical eddy heat fluxes. Gutowski et al. (1989) showed that, in a quasi-linear model, both of these processes contribute about equally to adjusting the mean flow. Moreover, when the vertical temperature profile was calculated internally, there was less modification of the meridional temperature gradient than when the static stability was fixed. Also, Zhou and Stone (1993) showed with a spherical nonlinear two-level model that forcing of the mean flow by vertical eddy heat fluxes is more than half as large as by the meridional eddy heat fluxes, and thus not negligible. Our model, therefore, may overestimate the change in the meridional temperature gradient relative to the real atmosphere. However, these last authors also demonstrated a few key ways in which the fixed versus variable nature of the static stability was not paramount. Their equilibrium state, by several different measures, did not change much in going from a varying to a constant value of the Brunt–Väisälä frequency. In addition, the heat flux spectra resulting from the upscale cascade were similar in the two cases (their Fig. 9). Thus, we have neglected here the complication due to variable static stability in order to focus on the interaction of horizontal heat transport and the horizontal temperature profile, consistent with the quasigeostrophic formulation adopted. In the future our results should be tested with a model that allows for vertical heat fluxes and variation of the vertical temperature profile.

We have used quasigeostrophic scaling in our formulation, which is based on the Rossby number being small: $\mathrm{Ro} \equiv U/f_0L \ll 1$. However, as the driving increases the advective timescale, L/U becomes small. The

underlying expansion in Ro will not be valid, and hence neither will be our model output at very high forcings. This issue and that of fixed static stability are the main limitations of the model.

The value of the Newtonian cooling parameter h'' in this study has been set at 56 days. As in Welch and Tung (1998), this very slow value has been chosen because it elucidates the dynamics of the different waves. Simulations with a more realistic value of 18 days yield the same qualitative behavior, but the different waves are difficult to distinguish one from another.

Finally, there is an issue as to how a channel model, having rigid walls, can be physically realistic for our study. Do the rigid walls introduce spurious dynamics into the problem? Consider Fig. 14b, which shows components of the zonal-mean thermodynamic energy equation (3.4) at equilibrium for the wintertime case of $\Delta T^{\dagger} = 90$ K. There are indeed boundary layers in the vertical velocity $\overline{\omega}_2$ and the heat flux convergence Π, forced by our choice of streamfunction to satisfy the no-flow boundary conditions at the walls. However, what determines the resultant equilibrium is neither of these components separately but rather their sum, in the form of the transformed Eulerian mean (TEM), defined by: $\overline{\omega}_2^* \equiv \overline{\omega}_2 - (\delta/2\sigma_0)\partial(\overline{v_2'T_2'})/\partial y$, where the asterisk indicates the TEM. From (3.4) at equilibrium we then have

$$\overline{T}_{2,\mathrm{eq}} \approx T^{\dagger} + \frac{\sigma_0}{h''}\overline{\omega}_2^*. \tag{5.1}$$

One can see from Fig. 14b that the net effect of the TEM is to modulate the forced temperature $T^{\dagger}$, from its large amplitude to a smaller amplitude in $\overline{T}_{\mathrm{eq}}$, while retaining the cos$y$ profile. No boundary layers are created in $\overline{T}_{\mathrm{eq}}$. Thus our sidewall boundary conditions are not introducing artificial dynamics into the results. Note that we could have taken a different modeling approach, pushing the meridional boundaries far away from the center of the channel so that there is only negligible eddy activity at the walls. Instead, we have chosen to use a channel width more akin to the real midlatitudes in our study, drawing on evidence from other authors that channel models with ''near'' walls that confine disturbances can accurately simulate baroclinic dynamics on a rotating sphere, in which the midlatitude jet acts as a waveguide (Yang et al. 1997). It is interesting and encouraging that we have obtained some similar results to those produced by models designed to be homogeneous and isotropic (e.g., Haidvogel and Held 1980). Both types of models are no doubt important tools of discovery for this problem.

6. Summary and conclusions

We have shown that the theory of nonlinear baroclinic adjustment can explain the maximum in the spectrum of meridional heat flux versus zonal wavenumber. Starting with the most unstable wave from a linear stability analysis, successively longer and longer waves grow and transport heat until they reach their nonlinear saturation threshold, at which point they break and pass off excess energy upscale. The largest heat flux occurs at the longest wave that grows but does not saturate. This wave acts as the atmosphere's thermostat, reducing the meridional temperature gradient down to a level that is linearly critical with respect to that wave. As the forcing is increased, the cascade of energy results in a longer and longer wave dominating. However, because the critical gradients of many synoptic waves are similar in magnitude, the resultant temperature gradient varies very little over a wide range of forcing, a feature which is also seen season-to-season in our current climate. This is true even though the dominant wave shifts by five or six wavenumbers as the forcing rises.

The synoptic maximum in the spectrum of perturbation energy can also be explained by this mechanism, as it is virtually the same as the heat flux maximum. The theory predicts an m^{-4} shape of the heat flux spectrum and approximately m^{-3} for the energy spectrum, which are corroborated by model simulations and (for the heat flux) observations.

Combined with the results of Welch and Tung (1998), the nonlinear baroclinic adjustment mechanism has been shown to work through a broad region of parameter space, explaining the equilibration of baroclinic flows with any number of waves unstable and over a wide range of forcings. This mechanism can account for the observed flexibility of meridional eddy heat transport in the atmosphere. An important part of the theory is that waves can be stabilized by different methods, linear and nonlinear, so that not all waves must be linearly stabilized in order to achieve an equilibrium.

Acknowledgments. WTW's research has been supported in part by NSF through its sponsorship of NCAR, in part by NASA under its Global Change Fellowship Program under Grant 1812-GC92-0169, and in part by the following grant; KKT's research is supported by NSF's Climate Dynamics Program under Grant ATM-9526136. WTW would also like to thank Rol Madden, Bill Randel, and Joe Tribbia for their aid in preparing this work.

REFERENCES

Cehelsky, P., and K. Tung, 1991: Nonlinear baroclinic adjustment. *J. Atmos. Sci.,* **48,** 1930–1947.

Charney, J. G., 1971: Geostrophic turbulence. *J. Atmos. Sci.,* **28,** 1087–1095.

——, and P. Drazin, 1961: Propagation of planetary-scale disturbances from the lower into the upper atmosphere. *J. Geophys. Res.,* **66,** 83–109.

——, and M. Stern, 1962: On the stability of internal baroclinic jets in a rotating atmosphere. *J. Atmos. Sci.,* **19,** 159–172.

DelSole, T., and B. Farrell, 1995: A stochastically excited linear system as a model for quasigeostrophic turbulence: Analytical results for one- and two-layer fluids. *J. Atmos. Sci.,* **52,** 2531–2547.

——, and ——, 1996: The quasi-linear equilibration of a thermally maintained, stochastically excited jet in a quasigeostrophic model. *J. Atmos. Sci.,* **53,** 1781–1797.
Farrell, B. F., 1982: The initial growth of disturbances in a baroclinic flow. *J. Atmos. Sci.,* **39,** 1663–1686.
——, 1989: Optimal excitation of baroclinic waves. *J. Atmos. Sci.,* **46,** 1193–1206.
——, and P. Ioannou, 1994: A theory for the statistical equilibrium energy spectrum and heat flux produced by transient baroclinic waves. *J. Atmos. Sci.,* **51,** 2685–2698.
——, and ——, 1995: Stochastic dynamics of the midlatitude atmospheric jet. *J. Atmos. Sci.,* **52,** 1642–1656.
Gall, R., 1976: A comparison of linear baroclinic instability theory with the eddy statistics of a general circulation model. *J. Atmos. Sci.,* **33,** 349–373.
Garcia, R. R., 1991: Parameterization of planetary wave breaking in the middle atmosphere. *J. Atmos. Sci.,* **48,** 1405–1419.
Gutowski, W., L. E. Branscome, and D. Stewart, 1989: Mean flow adjustment during life cycles of baroclinic waves. *J. Atmos. Sci.,* **46,** 1724–1737.
Haidvogel, D., and I. Held, 1980: Homogeneous quasi-geostrophic turbulence driven by a uniform temperature gradient. *J. Atmos. Sci.,* **37,** 2644–2660.
Held, I., 1978: The vertical scale of an unstable wave and its importance for eddy heat flux parameterizations. *J. Atmos. Sci.,* **35,** 572–576.
James, I., 1987: Suppression of baroclinic instability in horizontally sheared flows. *J. Atmos. Sci.,* **44,** 3710–3720.
Larichev, V. D., and I. Held, 1995: Eddy amplitudes and fluxes in a homogeneous model of fully developed baroclinic instability. *J. Phys. Oceanogr.,* **25,** 2285–2297.
Lilly, D., 1972: Numerical simulation study of two-dimensional turbulence. *Geophys. Astrophys. Fluid Dyn.,* **3,** 289–319.
Lindzen, R., 1993: Baroclinic neutrality and the tropopause. *J. Atmos. Sci.,* **50,** 1148–1151.
——, 1994: The Eady problem for a basic state with zero pv gradients but $\beta \neq 0$. *J. Atmos. Sci.,* **51,** 3221–3226.
Lorenz, E., 1960: Energy and numerical weather prediction. *Tellus,* **12,** 364–373.
Panetta, R., 1993: Zonal jets in wide baroclinically unstable regions: Persistence and scale selection. *J. Atmos. Sci.,* **50,** 2073–2106.
Pavan, V., 1996: Sensitivity of a multi-layer quasi-geostrophic β-channel model to the vertical structure of the equilibrium meridional temperature gradient. *Quart. J. Roy. Meteor. Soc.,* **122,** 55–72.
——, and I. Held, 1996: The diffusive approximation for eddy fluxes in baroclinically unstable jets. *J. Atmos. Sci.,* **53,** 1262–1272.
Pedlosky, J., 1987: *Geophysical Fluid Dynamics.* 2d ed. Springer-Verlag, 710 pp.
Peixoto, J., and A. Oort, 1992: *Physics of Climate.* American Institute of Physics, 520 pp.
Randel, W., and I. Held, 1991: Phase speed spectra of transient eddy fluxes and critical layer absorption. *J. Atmos. Sci.,* **48,** 688–697.
Rhines, P., 1975: Waves and turbulence on a beta-plane. *J. Fluid Mech.,* **69,** 417.
Salmon, R., 1980: Baroclinic instability and geostrophic turbulence. *Geophys. Astrophys. Fluid Dyn.,* **15,** 167–211.
Solomon, A. B., 1997: An observational study of the spatial and temporal scales of transient eddy sensible heat fluxes. *J. Climate,* **10,** 508–520.
Stone, P., 1978: Baroclinic adjustment. *J. Atmos. Sci.,* **35,** 561–571.
Tanaka, H., and E. Kung, 1988: Normal mode energetics of the general circulation during the FGGE Year. *J. Atmos. Sci.,* **45,** 3723–3736.
Wallace, J. M., and P. Hobbs, 1977: *Atmospheric Science.* Academic Press, 467 pp.
Welch, W., 1996: Nonlinear baroclinic adjustment and wavenumber selection as a mechanism for atmospheric heat transport. Ph.D. thesis, University of Washington, 131 pp.
——, and K. Tung, 1998: Nonlinear baroclinic adjustment and wavenumber selection in a simple case. *J. Atmos. Sci.,* **55,** 1285–1302.
Whitaker, J., and A. Barcilon, 1995: Low frequency variability and wavenumber selection in models with zonally symmetric forcing. *J. Atmos. Sci.,* **52,** 491–503.
Willson, M. A. G., 1975: A wavenumber-frequency analysis of large-scale tropospheric motions in the extratropical Northern Hemisphere. *J. Atmos. Sci.,* **32,** 478–488.
Yang, S., B. Reinhold, and E. Kallen, 1997: Multiple weather regimes and baroclinically forced spherical resonance. *J. Atmos. Sci.,* **54,** 1397–1409.
Zhou, S., and P. H. Stone, 1993: The role of large-scale eddies in the climate equilibrium. Part II: Variable static stability. *J. Climate,* **6,** 1871–1881.